In vitro Analysis of Localized Aneurysm Rupture

Aaron Romo, Pierre Badel, Ambroise Duprey, Jean-Pierre Favre, Stéphane
Avril

▶ To cite this version:

HAL Id: hal-01025664
https://hal.science/hal-01025664

In vitro Analysis of Localized Aneurysm Rupture

Aaron Romo[1], Pierre Badel[1], Ambroise Duprey[2], Jean-Pierre Favre[2], Stéphane Avril[1]

[1] Ecole Nationale Supérieure des Mines de Saint-Etienne, CIS-EMSE, CNRS:UMR5146, LCG, F-42023 Saint Etienne, France

[2] Hôpital Nord, Cardiovascular Surgery Service, CHU de Saint Etienne, F-42055 Saint-Etienne cedex 2, France.

Corresponding author:

Aaron Romo

Center for Health Engineering

Ecole Nationale Supérieure des Mines

158 cours Fauriel

42023 SAINT-ETIENNE CEDEX 2 France

Phone: +33477429329

Fax: +33477499755

Email: romo@emse.fr

KEYWORDS

Aneurysm, human aorta, inflation test, rupture, ultimate stress.

word count (introduction through acknowledgments): 3511

ABSTRACT

In this study, bulge inflation tests were used to characterize the failure response of 15 layers of human ascending thoracic aortic aneurysms (ATAA). Full field displacement data were collected during each of the mechanical tests using a digital image stereo-correlation (DIS-C) system. Using the collected displacement data, the local stress fields at burst were derived and the thickness evolution was estimated during the inflation tests. It was shown that rupture of the ATAA does not systematically occur at the location of maximum stress, but in a weakened zone of the tissue where the measured fields show strain localization and localized thinning of the wall. Our results are the first to show the existence of weakened zones in the aneurysmal tissue when rupture is imminent. An understanding these local rupture mechanics is necessary to improve clinical assessments of aneurysm rupture risk. Further studies must be performed to determine if these weakened zones can be detected *in vivo* using non-invasive techniques.

INTRODUCTION

Each year thoracic aneurysms are diagnosed in approximately 15,000 people in the United States and more than 30,000 people in Europe (Clouse 1998). Of this number 50-60% are ascending thoracic aortic aneurysms (ATAA) (Isselbacher 2005). However the rupture of the ATAA remains an almost unexplored topic. ATAAs are caused by the remodeling of the arterial wall and they rupture when the stress applied to the aortic wall locally exceeds its capacity to sustain stress (Vorp et al., 2003).

In an attempt to understand the mechanical behavior of the aortic tissue; different authors have performed mechanical tests. Uniaxial tensile tests were performed by (Mohan and Melvin, 1982) on healthy descending aortic specimens; they concluded that the most reasonable failure theory for aortic tissue was the maximum tensile strain theory. (He and Roach, 1994) also performed uniaxial tensile tests and showed that aneurysms were less distensible and stiffer than healthy tissues. Using uniaxial tensile tests to compare healthy tissues with ATAA specimens (Garcia-Herrera et al., 2011) concluded that the age, beyond the age of 35, was the cause of significant decrease of rupture load and elongation at failure. They found no significant differences between the mechanical strength of aneurysms and healthy tissues. In contrast, (Vorp et al., 2003) found a significant decrease in the tensile strength of the ATAA specimens and concluded that its formation was associated with the stiffening and weakening of the aortic wall. Providing data on the mechanical behavior in the physiological range, (Duprey et al., 2010) found that the aortic wall was significantly anisotropic with the circumferentially oriented samples being stiffer than the axial ones.

The biaxial mechanical behavior of the aortic tissue has been investigated with bulge inflation tests. Dynamic and quasi-static bulge inflation tests (Mohan and Melvin, 1983) were performed on healthy descending aortas. The failure of the aortic tissue always took place with a tear in the circumferential direction. Similarly, (Marra et al., 2006) performed inflation tests using porcine healthy aortic tissues,

76 showing that the rupture occurs with a crack oriented in the circumferential direction of the artery.

77 More recently (Kim et al., 2012) performed inflation tests using ATAA specimens. Material

78 parameters were identified using the virtual fields method (Grédiac et al., 2006; Avril et al., 2010)

79 and the average Cauchy stress values at which the rupture occurred were derived for all the

80 specimens.

81

82 None of the studies mentioned above analyzed locally the rupture of the tissue from its first

83 initiation. Moreover, all these studies derived an average stress estimation across the specimens and

84 none were able to show if the rupture initiates at the location of maximum stress or if the rupture

85 was triggered by the existence of weakened parts within the tissue. Our objective was to address

86 this issue by carrying out full-field measurements in human ATAA specimens tested in a bulge

87 inflation test up to failure. In order to determine the cause and location of the rupture, thickness

88 evolution estimations and local stress distributions were calculated during the inflation of the

89 specimens.

90
91

METHODS

Sample Preparation and Experimental Protocol

ATAA specimens were obtained from donor patients who underwent surgical replacement of their ATAA with a synthetic graft. The collection of the aortic tissues was done in accordance with the guidelines of the Institutional Review Board of the University Hospital Center of Saint-Etienne. Specimens were kept at 4 °C in 0.9% physiological saline solution and testing was completed within 24 hours of tissue harvest (Adham et al. 1996). Table 1 lists the demographic information for the collected ATAA specimens.

Each ATAA (Fig. 1-a) was cut into square specimen approximately 45 x 45 mm. Each specimen was then separated into two layers: intima-media and adventitia (Fig. 1-b). The average thickness of each layer was measured using digital calipers; the layer of interest was put between two plastic plates and the thickness of the layer and the plates was measured. Then the thickness of the two plates was subtracted from the measured value. The ATAA layer was clamped in the inflation device so that the luminal side of the tissue faced outward and the circumferential direction of the artery coincided with the horizontal axis of the clamp (Fig. 1-c). Finally a speckle pattern was applied to each sample using black spray paint (Fig. 1-c). Note that the luminal side of each layer was chosen to face outward since the adventitial surface was highly irregular making difficult for the speckle pattern to adhere to the surface.

A hermetically sealed cavity was formed between the clamped ATAA layer and the inflation device. During the inflation test, water was injected at a constant rate by pushing a piston pump at 15 mm/min until the tissue ruptured. Simultaneously, the pressure was measured with a digital manometer (WIKA®, pressure gauge DG-10). Images were recorded using a commercial DIS-C system (GOM®, ARAMIS 5M LT) at every 3 kPa, until the sample ruptured (Fig. 2). The DIS-C system was

118   composed of two 8-bit CCD cameras equipped with 50 mm lenses (resolution: 1624 x 1236 px). In

119   this study, 15 ATAA layers were successfully tested until rupture. Only the specimens that ruptured in

120   their central area (without touching the boundaries of the inflation device) were used.

121

122   ***Data Analysis***

123   Once the experimental procedure was completed, image processing was performed using Aramis®

124   software. In each of the acquired images (Fig. 2), the area of interest (AOI), which was a circle

125   measuring 30 mm diameter, was identified. A facet size of 21 px and a facet step of 5 px were chosen

126   based on the speckle pattern dot size, distribution, and contrast. The selected facet size and step

127   yielded a resolution of 0.54 μm for in-plane displacements and 1.5 μm for the out-of-plane

128   displacement.

129

130   To capture the kinematics of the membrane (Naghdi 1972; Green and Adkins 1970; Lu et al., 2008)

131   we define the position vectors for a material point P in the initial and deformed configurations as

132    $X(P)$ and $x(P)$, respectively (Fig. 4). The surface is parameterized using a pair of surface coordinates

133    $\xi^\alpha(P) = X(P) \cdot E_\alpha$ where E_α are the basis vectors of the global coordinate system GCS (Fig. 3) and

134    $\alpha = 1,2$. The local covariant basis vectors g_α and G_α for the deformed and initial configurations,

135   respectively, are found using the following relationships:

136

$$g_\alpha = \frac{\partial x}{\partial \xi^\alpha} \qquad\qquad G_\alpha = \frac{\partial X}{\partial \xi^\alpha} \qquad (1)$$

137

138   The local contravariant basis vectors g^α and G^α are then defined as:

139

$$g^\alpha = \frac{\partial \xi^\alpha}{\partial x} \qquad\qquad G^\alpha = \frac{\partial \xi^\alpha}{\partial X} \qquad (2)$$

140

141   The two-dimensional deformation gradient, F, is calculated from the current and initial basis vectors:

142

$$F = \; g_\alpha \otimes G^\alpha \tag{3}$$

143

144   Then, at each material point, the two- dimensional Green-Lagrange strain, E, is determined:

145

$$E = \frac{1}{2}(F^T F - I) \tag{4}$$

146

147   To define the three-dimensional deformation, we set $\lambda_3 = h/h_0$, where h and h_0 are the thicknesses

148   in the deformed and undeformed configurations, respectively, and required the transverse shear

149   strains to vanish. It follows that the three dimensional deformation gradient and Green-Lagrange

150   strain tensor are given by:

151

$$F = \; g_\alpha \otimes G^\alpha + \lambda_3 \, n \, \otimes N \qquad E = \frac{1}{2}\big(g_{\alpha\beta} \, G^\alpha \otimes G^\beta + \lambda_3{}^2 \, N \, \otimes N - I\big) \tag{5}$$

152

153   where n and N are outward unit normals to the surface in the current and initial configurations,

154   respectively.

155

156   ***Determination of the Local Stress Fields***

157   The aneurysm wall is modeled as a nonlinear elastic membrane. A unique feature of modeling the

158   aneurysm wall as a nonlinear elastic membrane is that the tension in the vessel wall can be

159   determined *without* the use of a constitutive model to describe the elastic properties of the wall (Lu

160   et al., 2008). The local equilibrium equations for the elastostatic problem may be written as (Lu et

161   al., 2008; Zhao 2009):

162

$$\frac{1}{\sqrt{g}} \left(\sqrt{g} h \sigma^{\alpha\beta} \boldsymbol{g}_\alpha \right)_{,\beta} + p\boldsymbol{n} = \boldsymbol{0} \qquad (6)$$

163

164 where $g = \det(\boldsymbol{g}_\alpha . \boldsymbol{g}_\beta)$ is the determinant of the metric tensor, h is the current thickness, p is the

165 internal pressure applied for the inflation and $\sigma^{\alpha\beta}$ are the unknown components of the Cauchy

166 stress tensor $\boldsymbol{\sigma}$ in the local covariant basis. Note that Eq. (6) is in tensorial form and the Einstein

167 summation convention is used. Then, we approximate the spatial variations of all the quantities of

168 Eq. (6) using linear shape functions of the surface coordinates which take on a null value at all nodes

169 of the mesh except at node k where it is 1. The shape functions are defined on a triangular finite

170 element mesh having N elements and K nodes (Fig. 5).

171

172 Using this approximation scheme, Eq. (6) is written at the centroid of each element, which yields:

173

$$\frac{1}{\frac{1}{3}\sum_{k=1}^{3}\sqrt{g(\boldsymbol{x}_k)}} \sum_{k=1}^{3} \left[\sqrt{g(\boldsymbol{x}_k)} h(\boldsymbol{x}_k) \sigma^{\alpha\beta}(\boldsymbol{x}_k) \boldsymbol{g}_\alpha(\boldsymbol{x}_k) \frac{d\varphi_k}{d\xi^\beta} \right] + p\frac{1}{3}\sum_{k=1}^{3} \boldsymbol{n}(\boldsymbol{x}_k) = \boldsymbol{0} \qquad (7)$$

174

175 where $\frac{d\varphi_k}{d\xi^\beta}$ are the shape function derivatives at the centroid of the element and where the Einstein

176 summation convention still applies for indexes α and β. Eq. (7) is then projected into the GCS and the

177 procedure is repeated for each triangular element. A linear system of $3N$ equations is produced. It

178 contains $3K$ unknowns which are the 3 components of the Cauchy stress tensor in the local covariant

179 basis at the K nodes of the mesh. A convergence study showed that a mesh with N=1203 elements

180 and K=644 nodes was a good compromise between precision and time of calculation.

181

182 The system was completed by a set of equations on the boundaries of the tested area, where it was

183 assumed:

184

$$(\boldsymbol{\sigma} \cdot \boldsymbol{j}) \cdot \boldsymbol{n} = 0 \qquad (8)$$

$$(\boldsymbol{\sigma} \cdot \boldsymbol{j}) \cdot \boldsymbol{i} = 0 \qquad (9)$$

185

186 where $\boldsymbol{i}, \boldsymbol{j}, \boldsymbol{n}$ defines a local basis at the boundaries (Fig. 5-b) with i is tangent to the boundary, $\boldsymbol{n}$ is

187 an outward unit normal vector to the surface and $\boldsymbol{j} = \boldsymbol{n} \otimes \boldsymbol{i}$ is chosen to make the local coordinate

188 system right-handed. Along the boundaries, Eq. (8) sets the traction vector perpendicular to ,

189 allowing in-plane tractions only and Eq. (9) sets the traction vector perpendicular to i , allowing no

190 shear on the boundary. The resultant boundary traction automatically balances the total pressure

191 applied on the wall due to the local equilibrium equation (Eq. (6)) written for each element. The final

192 over-determined linear system of equations was solved in the least-squares sense.

193

194 The calculated components of the stress tensor are finally projected in the orthonormal local

195 coordinate system (LCS) ($\boldsymbol{e_1}, \boldsymbol{e_2}, \boldsymbol{e_3}$) defined such that:

196

$$\boldsymbol{e_3} = \boldsymbol{n}$$
$$\boldsymbol{e_2} = \frac{\boldsymbol{g_2}}{\|\boldsymbol{g_2}\|} \qquad (10)$$
$$\boldsymbol{e_1} = \boldsymbol{e_2} \otimes \boldsymbol{e_3}$$

197

198 where $\boldsymbol{n}$ is again the outward unit normal to the surface.

199

200 The stress was analyzed at three locations:

201

202 • NodeMAX: node with the largest stress eigenvalue

203 • NodeTOP: node at the top of the inflated membrane

204 • NodeRUP: node where rupture initiates

205

206   At NodeMAX and NodeTOP locations, the largest eigenvalue of the Cauchy stress tensor (largest

207   principal stress) were found and denoted σ^{Max} and σ^{Top}, respectively. At NodeRUP, the stress in the

208   direction perpendicular to the crack that occurs at rupture was computed:

209

$$\sigma^{Rup} = (\boldsymbol{\sigma} \cdot \boldsymbol{q}_\theta) \cdot \boldsymbol{q}_\theta \qquad\qquad (11)$$

210

211   where $\boldsymbol{q}_\theta$ is the unit vector perpendicular to the rupture (Fig. 8c). It is derived for each specimen

212   using the images obtained from the DIS-C system at the moment of the rupture. Using a custom

213   MatLab® code, a series of points were manually placed on an image of the ruptured edge. A linear

214   regression was then performed using those points and the angle between the fit line and the

215   horizontal axis was calculated.

216

217   *Finite Element Validation Study*

218   Using a mesh size of N=1203 elements and K=644 nodes, a validation analysis was performed (see

219   Appendix A for details). The stress distributions obtained from a finite element analysis (FEA) were

220   defined as reference values and compared with the stress distributions obtained using the present

221   approach.

222

223   *Thickness Evolution*

224   At every pressure step, the current thickness of each element was calculated. The aneurysmal tissue

225   was modeled as incompressible membrane therefore the following relationship holds between the

226   initial thickness, h_0, and the current thickness, h.

227

$$h = \frac{h_0}{F_{11}F_{22} - F_{21}F_{12}} \qquad (12)$$

228

229   We note that the *ex vivo* thickness, h_0, was assumed to be initially homogeneous and that F_{11}, F_{22},

230   F_{21} and F_{12} are the components of the deformation gradient tensor (Eq. (3)).

231

232   ***Laplace's Law***

233   Laplace's Law (Peterson et al., 1960; Humphrey 2002) was used to calculate a global estimate of the

234   ultimate stress for each ATAA layer by assuming the sample was a hemisphere

235

$$\sigma^{Lap} = \frac{pr}{2h} \qquad (13)$$

236

237   where p was the inflation pressure, r was the radius of curvature estimated using a least-squares

238   surface fitting of the inflated shape, and h was the average current thickness of the elements in the

239   mesh.

240

241

242   **RESULTS**

243

244   The stress distributions obtained from the FEA simulation (Fig. 6-a) were compared with the stress

245   distributions obtained using the present approach (Fig. 6-b). The mean absolute error (Fig. 6-c) was

246   calculated revealing that the largest errors occurred at the boundaries. Ignoring the elements at the

247   boundaries, the average error was significantly reduced to 0.8%, 1.4%, and 0.8% for σ_{11}, σ_{22}, and

248   σ_{12}, respectively (Fig. 6-d). This showed that the stress estimates contain some errors along the

249   border due to the assumed boundary conditions but these errors vanish rapidly away from the

250   border. For this reason, only the tests where the rupture occurred at a distance of more than three

251 elements away from the border were included in this study.

252

253 Using the approach we have presented, the components of the Cauchy stress tensor were calculated

254 at every node for each 3 kPa pressure step until the sample ruptured (Fig. 7-a). The displacement

255 (Fig. 7-b) and strain fields (Fig. 7-c) used to calculate the stress and thickness evolution are also

256 shown.

257

258 In Table 2 we report the three components of the Cauchy stress tensor. Our results (mean ± std) for

259 σ_{11} were 1.18 ±0.64 MPa at NodeMAX, 1.12 ±0.64 MPa at NodeTOP and 1.06 ±0.59 MPa at

260 NodeRUP. The values for σ_{22} were 1.21 ±0.80 MPa at NodeMAX, 1.17 ±0.79 MPa at NodeTOP and

261 1.05 ±0.71 MPa at NodeRUP.

262

263 In Fig. 8-a, we show the thickness distribution (Eq. (12)) one pressure step before rupture for five

264 tests. For each of the samples thick (dark red) and thin (dark blue) regions can be identified. The

265 locations of NodeMAX, NodeTOP, and NodeRUP for these five tests are also shown in Fig. 8-b.

266 Contrary to the generally accepted theory that the rupture occurs at the location of the maximum

267 stress, the experimental results show that rupture often initiates at a different location (NodeRUP),

268 possibly due to the non-homogeneous strength of the tissue. An image of the ruptured layer is

269 shown in Fig. 8-c, where the magenta points and the blue regression line were used to determine the

270 rupture angle, θ.

271

272 Table 3 and Fig. 9 summarize the three ultimate stress values (σ^{Max}, σ^{Top}, and σ^{Rup}) calculated at

273 their corresponding locations (NodeMAX, NodeTOP and NodeRUP) compared with σ^{Lap} (Eq. (13)).

274 For the six adventitia layers, the average stress values (mean ± std) were 1.49 ±1.06 MPa, 1.76 ±1.07

275 MPa, 1.69 ±1.10 MPa, and 1.46 ±1.03 MPa for σ^{Lap}, σ^{Max}, σ^{Top}, and σ^{Rup}, respectively. For the

276 remaining nine media layers, the average stress values were found to be 0.78 ±0.26 MPa, 1.01 ±0.36

277   MPa, 0.95 ±0.31 MPa, and 0.78 ±0.20 MPa for σ^{Lap}, σ^{Max}, σ^{Top}, and σ^{Rup}, respectively. The four

278   calculated ultimate stress values were higher for the adventitia layers, confirming its role of

279   structural support of the artery (Fung, 1993).

280

281

DISCUSSION

283

Comparison with Existing Literature

285   Other investigators performing inflation tests have reported rupture stresses between 0.751 and

286   1.75 MPa (Kim et al., 2012, Mohan and Melvin, 1983, Marra et al., 2006). In the present study the

287   rupture stress, σ^{Rup}, was on average 1.46 MPa for the adventitia layers and 0.72 MPa for the media

288   layers. The results obtained from our analysis were reasonable and lie within the range of reported

289   values in the literature. It must be noted that our results were twice as large of those of Kim et al.

290   (2012) who found 0.751 MPa for adventitia layers and 0.39 MPa for media layers. This can be

291   explained by the different methods used to calculate the rupture stress. While Kim et al. (2012)

292   assumed a constant thickness throughout the inflation, the present method was capable of

293   estimating the thickness evolution of the sample (Eq. (12)). Based on the large changes in thickness

294   observed in the samples (Fig. 10), it was expected that our values would be significantly larger than

295   those reported by Kim et al. (2012).

296

Comparison of the Ultimate Stress at Different Locations

298   The stress found using Laplace's Law, σ^{Lap}, in Eq. (13) was considered a global estimate of the

299   rupture stress, since it was computed using a global radius of curvature and the mean thickness of

300   the inflated ATAA layer. A comparison between this global stress value and the calculated local stress

301   values, σ^{Max}, σ^{Top}, and σ^{Rup}, was done as the majority of published studies have not calculated

302   local stress distributions. The stress calculated from Laplace's Law was frequently smaller than the

303 other local stress values. The difference can likely be explained by differences in the thickness

304 calculation. On the one hand Laplace's Law uses the average current thickness of the entire inflated

305 aortic layer while the three local stress values use the current local thickness of the element where

306 the node concerned was located.

307

308 **Detection of Weakened Zones in the Tissue**

309 In every test rupture was preceded by significant local deformation and reduction of the thickness.

310 This phenomenon was clearly illustrated in Fig. 8, where local thinning was observed at the rupture

311 location. Occasionally the maximum stress value was located in the weakened area, but more

312 frequently it was located elsewhere. This led us to hypothesize that the ATAA layers had weakened

313 regions that caused the localized thinning of the layer during the inflation test. When observing the

314 evolution of the ATAA layer thickness (Fig. 10), the region where the rupture was most likely to occur

315 could be observed many stages before the rupture. Moreover, the orientation of the rupture always

316 appeared in the same direction as the thickness heterogeneity in the inflated ATAA layer.

317

318 **Main Sources of Variability**

319 It was noticed that test number 2, an adventitia layer, had by far the highest ultimate stress values.

320 Possibly explained because this layer was the thinnest of all the tissue samples and the donor patient

321 was 36 years old, which made him by far the youngest patient donor (mean age: 66 years).

322

323 **Limitations**

324 *a) Comparison with healthy tissue*

325 Due to the difficulty of obtaining healthy ascending aortic specimens, there was no comparison

326 between healthy aorta and ATAA specimens. As many authors have noticed (Choudhury et al., 2008;

327 Cinthio et al., 2006; Prehn et al., 2009), this comparison can help understanding the causes of the

328 pathology.

14

329

b) *Initial thickness measurement*

331 The measurement of the *ex vivo* initial thickness h_0 of the ATAA tissue was an average estimate of

332 the thickness of the tissue. Measuring the thickness of the specimen at various locations in the tissue

333 was precluded as the sharp shape of the caliper can easily penetrate the soft tissue and damage the

334 tissue. The tests method could be further improved in the future by incorporating a technique

335 capable of capturing the location dependent thickness of the tissue. Other techniques such as, for

336 example, a PC-based video extensometer (Sommer et al., 2008) or a non-contact laser beam

337 micrometer (Iliopoulos et al., 2009) could be used to measure the thickness of the aortic tissue at

338 multiple locations.

339

c) *Effect of the loading conditions*

341 A finite element study was undertaken to show that the traction boundary conditions used in our

342 simulation (Eqs. 9-10) only minimally affected the stress calculations in the center region of the

343 specimen. Due to boundary effects, the present approach is limited to characterizing rupture

344 phenomenon occurring far from the boundaries. In the future it would be useful to improve the

345 precision by implementing an approach similar to Zhao (2009) who defined a boundary-effect-free

346 region where the calculated stress distribution remains invariant.

347

d) *Pure membrane assumption*

349 Using the present approach, the average stress across the thickness of the inflated ATAA layer was

350 calculated. The assumption of a pure membrane behavior is justified when the concerned tissue is

351 subjected to tensile extension, and is physically thin enough so the transverse shear and the across-

352 thickness stress variation are safely ignored (Horgan and Saccomandi 2003, Lu et al. 2008). Based on

353 the validation analysis (Appendix A), the stress distribution calculated using the present approach

354 was in very good agreement with the average stress distribution calculated between the outer and

15

355 inner surface using Abaqus® software. This indicates that the pure membrane assumption does not

356 affect the reconstruction of this average stress across the thickness.

357

358

359 CONCLUSIONS

360

361 In this manuscript, we have used a straight forward approach to investigate the *in vitro* rupture

362 behavior of ATAA layer during an inflation test. The main advantage of our approach was that local

363 stress field for the ATAA layer was obtained without requiring any material properties. Our results

364 showed that rupture in the ATAA inflated layers was more prone to occur in regions where the layer

365 was weakened. The majority of the time, rupture occurs where the thickness of the layer has been

366 reduced the most. Using maps of the local thickness as a function of pressure one can easily predict

367 the rupture location. Future studies must be conducted to determine if the localized thinning

368 observed in these experiments can also be observed *in vivo* using techniques such as magnetic

369 resonance imaging.

370

371

372 ACKNOWLEDGEMENTS

373

377

378

379 CONFLICT OF INTEREST

16

380

381   None

382

383

REFERENCES

385

386 Adham, M., Gournier, J., Favre, J., De La Roche, E., Ducerf, C., Baulieux, J., Barral, X., Pouyet, M.,
387   1996. Mechanical characteristics of fresh and frozen human descending thoracic aorta.
388   Journal of Surgical Reaserch, 64(1), 32-34.
389 Avril, S., Badel, P., Duprey, A., 2010. Anisotropic and hyperelastic identification of in vitro human
390   arteries from full-field measurements. Journal of Biomechanics 43(15), 2978-2985.
391 Choudhury, N., Bouchot, O., Rouleau, L., Tremblay, D., Cartier, R., Butany, J., Mongrain, R., Leask, R.,
392   2008. Local mechanical and structural properties of healthy and diseased human ascending
393   aorta tissue, Cardiovascluar Pathology 18, 83-91.
394 Cinthio, M., Ahlgren, A., Bergkvist, J., Jansson, T., Persson, H., Lindstrom, K., 2006. Longitudinal
395   mouvements and resulting shear strain of the arterial wall. American Journal of Physiology -
396   Heart and Circulatory Physiology 291, H394-H402.
397 Clouse, W., Hallett, J., Schaff, H., Gayari, M., Ilstrup, D., Melton, L., 1998. Improved prognosis of
398   thoracic aortic aneurysms: a population-based study. Journal of the American Medical
399   Association 280, 1926-1929.
400 Duprey, A., Khanafer, K., Schlicht, M., Avril, S., Williams, D., Berguer, R., 2010. In vitro
401   characterization of physiological and maximum elastic modulus of ascending thoracic aortic
402   aneurysms using uniaxial tensile testing. European Journal of Vascular and Endovascular
403   Surgery 39, 700-707.
404 Fung Y., 1993. Biomechanics: mechanical properties of living tissues. Springer, New York.
405 Garcia-Herrera, C., Atienza, J., Rojo, F., Claes, E., Guinea, G., Celentano, D., Garcia-Montero, C.,
406   Burgos, R., 2012. Mechanical behaviour and rupture of normal and pathological human
407   ascending aortic wall. Medical & Biological Engineering & Computing 50, 559-566.
408 Grédiac, M., Pierron, F., Avril, S., Toussaint, E., 2006. The virtual fields method for extracting
409   constitutive parameters from full-field measurements: a review. Strain 42(4), 233-253.
410 Green, A., and Adkins, J., 1970. Large elastic deformations. Clarendon Press, Oxford.
411 He, C.M., Roach, M.R., 1994. The composition and mechanical properties of abdominal aortic
412   aneurysms. Journal of Vascular Surgery 20, 6-13.
413 Holzapfel, G., Gasser, T., Ogden, R., 2000. A New Constitutive Framework for Arterial Wall Mechanics
414   and a Comparative Study of Material Models. Journal of Elasticity, 61(1), 1-48.
415 Horgan, C., and Saccomandi, G., 2003. A description of arterial wall mechanics using limiting chain
416   extensibility constitutive models. Biomechanics and modeling in mechanobiology 1(4), 251-
417   66.
418 Humphrey, J., 2002. Cardiovascular solid mechanics: cells, tissues, and organs. Springer, New York.
419 Iliopoulos, D., Deveja, R., Kritharis, E., Perrea, D., Sionis, G., Toutouzas, K., Stefanadis, C., Sokolis, D.,
420   2009. Regional and directional variations in the mechanical properties of ascending thoracic
421   aortic aneurysms. Medical Engineering & Physics 31, 1-9.
422 Isselbacher, E., 2005. Thoracic and abdominal aortic aneurysms. Circulation 111, 816-828.
423 Kim, J., Avril, S., Duprey, A., Favre, J., 2012. Experimental characterization of rupture in human aortic
424   aneurysms using a full-field measurements technique. Biomechanics and Modeling in
425   Mechanobiology 6, 841-853.

426 Lee, J., Langdon, S., 1996. Thickness measurement of soft tissue biomaterials: a comparison of five
427   methods. Journal of Biomechanics 29(6), 829-832.
428 Lu, J., Zhou, X., Raghavan, M., 2008. Inverse method of stress analysis for cerebral aneurysms.
429   Biomechanics and Modeling in Mechanobiology 7, 477-486.
430 Marra, S., Kennedy, F., Kinkaid, J., Fillinger, M., 2006. Elastic and rupture properties of porcine aortic
431   tissue measured using inflation testing. Cardiovascular Engineering 6(4), 123-131.
432 Mohan, D., Melvin, J., 1982. Failure properties of passive human aortic issue. I—uniaxial tension
433   tests. Journal of Biomechanics 15, 887-902.
434 Mohan, D., Melvin, J., 1983. Failure properties of passive human aortic tissue. II—biaxial tension
435   tests. Journal of Biomechanics 16, 31-44.
436 Naghdi, P., 1972. The Theory of Shells and Plates. In: C. Truesdell (ed.) Encyclopedia of Physics.
437   Springer, New York.
438 Peterson, L., Jenesen, R., Parnell, J., 1960. Mechanical properties of arteries in vivo. Circulation
439   Research 8, 622-639.
440 Prehn, J., Herwaarden, J., Vincken, K., Verhagen, H., Moll, F., Bartels, L., 2009. Asymmetric aortic
441   expansion of the aneurysm neck: Analysis and visualization of shape changes with
442   electrocardiogram-gated magnetic resonance imaging. Journal of Vascular Surgery 49, 1395-
443   1402.
444 Sommer, G., Gasser, T., Regitnig, P., Auer, M., Holzapfel, G., 2008. Dissection properties of the human
445   aortic media : an experimental study. ASME Journal of Biomechanical Engineering 130,
446   021007-1 - 021007-12.
447 Vorp, D., Schiro, B., Ehrlich, M., Juvonen, T., Ergin, M., Griffith, B., 2003. Effect of aneurysm on the
448   tensile strength and biomechanical behavior of the ascending thoracic aorta. The Annals of
449   Thoracic Surgery 75(4), 1210-1214.
450 Zhao, X., 2009. Pointwise identification of elastic properties in nonlinear heterogeneous membranes,
451   and application to soft tissues. Dissertation, University of Iowa. http://ir.uiowa.edu/etd/222.

List of Tables

Table

452
453
454
455
456
457
458
459
460
461
462
463
464
465
466
467
468
469
470
471
472
473
474
475
476
477
478
479
480
481
482

483

484

TABLE 1. Demographic information for the collected ATAA specimens.

Test No.	Layer Type	Sex/Age	Diameter before surgery (mm)	*Ex vivo* thickness (mm)
1	adventitia	M/67	50	1.18
2	adventitia	M/36	50	0.51
3	adventitia	M/55	53	0.79
4	adventitia	M/81	54	0.64
5	adventitia	M/76	52	0.62
6	adventitia	M/71	48	0.55
7	media	M/70	63	0.89
8	media	M/67	50	0.68
9	media	M/54	60	0.98
10	media	M/55	53	1.09
11	media	F/76	55	1.15
12	media	M/81	54	0.91
13	media	M/68	59	1.02
14	media	M/69	51	1.09
15	media	M/71	48	1.04

TABLE 2. Components of the Cauchy stress tensor reported at the NodeMAX, NodeTOP and NodeRUP locations (in MPa). Test No. 1 to 6 were adventitia layers and Test No. 7 to 15 were media layers.

Test No.	NodeMAX			NodeTOP			NodeRUP		
	σ_{11}	σ_{22}	σ_{12}	σ_{11}	σ_{22}	σ_{12}	σ_{11}	σ_{22}	σ_{12}
1	1.124	1.091	-0.036	0.681	0.842	-0.098	1.128	1.062	-0.005
2	3.066	3.812	-0.065	3.035	3.778	-0.064	2.954	3.527	0.084
3	1.233	1.613	-0.011	1.246	1.554	0.023	0.977	0.949	0.189
4	0.938	0.853	0.001	0.922	0.863	-0.002	0.922	0.795	0.012
5	1.964	1.642	0.050	1.920	1.647	0.020	1.699	1.419	-0.042
6	1.035	1.019	-0.046	1.035	1.019	-0.046	0.920	0.933	-0.108
7	0.756	0.997	0.041	0.677	0.909	0.078	0.640	0.924	0.006
8	1.764	1.654	0.097	1.617	1.573	0.077	1.120	0.913	-0.051
9	1.042	1.064	-0.06	1.033	1.067	-0.05	0.903	1.049	-0.027
10	1.308	1.007	-0.012	1.042	1.038	-0.028	1.174	0.927	-0.042
11	0.627	0.622	-0.009	0.549	0.602	-0.03	0.552	0.605	-0.025
12	0.631	0.630	0.076	0.664	0.633	0.042	0.655	0.626	0.040
13	0.819	0.720	-0.055	0.805	0.714	-0.053	0.815	0.725	-0.051
14	0.728	0.866	-0.018	0.800	0.858	-0.016	0.791	0.805	0.0001
15	0.805	0.601	-0.037	0.79	0.588	-0.044	0.714	0.546	-0.041
Mean	**1.18**	**1.21**	**-0.006**	**1.12**	**1.17**	**-0.013**	**1.06**	**1.05**	**-0.004**
Std.	**0.64**	**0.80**	**0.05**	**0.64**	**0.79**	**0.05**	**0.59**	**0.71**	**0.06**

TABLE 3. Comparison between four different ultimate stress values calculated at different locations within the same tissue. Test No. 1 to 6 were adventitia layers and Test No. 7 to 15 were media layers.

Test No.	σ^{Lap} (MPa)	σ^{Max} (MPa)	σ^{Top} (MPa)	σ^{Rup} (MPa)
1	0.9695	1.1481	0.8889	1.0719
2	3.5825	3.8183	3.7841	3.5269
3	1.1725	1.6134	1.5558	0.9755
4	0.8116	0.9385	0.9222	0.8265
5	1.5928	1.9724	1.9221	1.4644
6	0.8414	1.0752	1.0752	0.9335
7	0.7275	1.0049	0.9337	0.6412
8	1.4016	1.8214	1.6756	1.0057
9	0.8503	1.1148	1.1036	0.9309
10	0.8215	1.3086	1.0692	1.1733
11	0.4863	0.6346	0.6169	0.6015
12	0.5559	0.7074	0.6936	0.6286
13	0.7283	0.8438	0.8302	0.7259
14	0.8244	0.8687	0.8623	0.8028
15	0.6386	0.8121	0.7994	0.5891
Mean	**1.0669**	**1.3121**	**1.2488**	**1.0598**
Std.	**0.7573**	**0.7979**	**0.7933**	**0.7236**
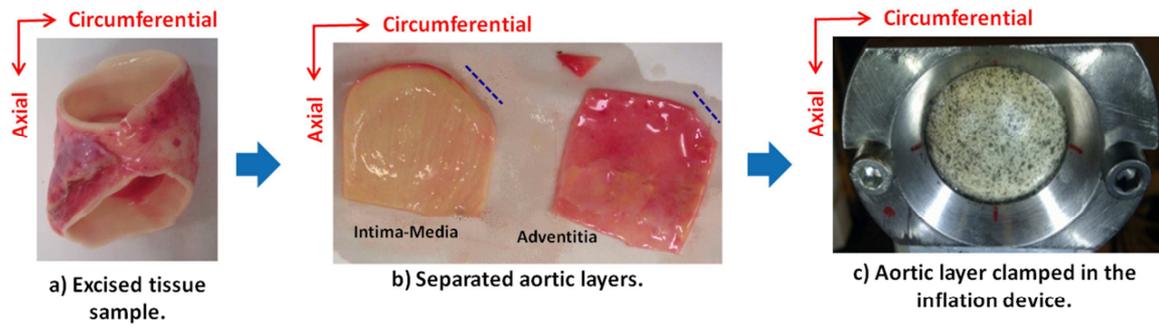
**Fig. 1.** ATAA specimen preparation for the inflation test.
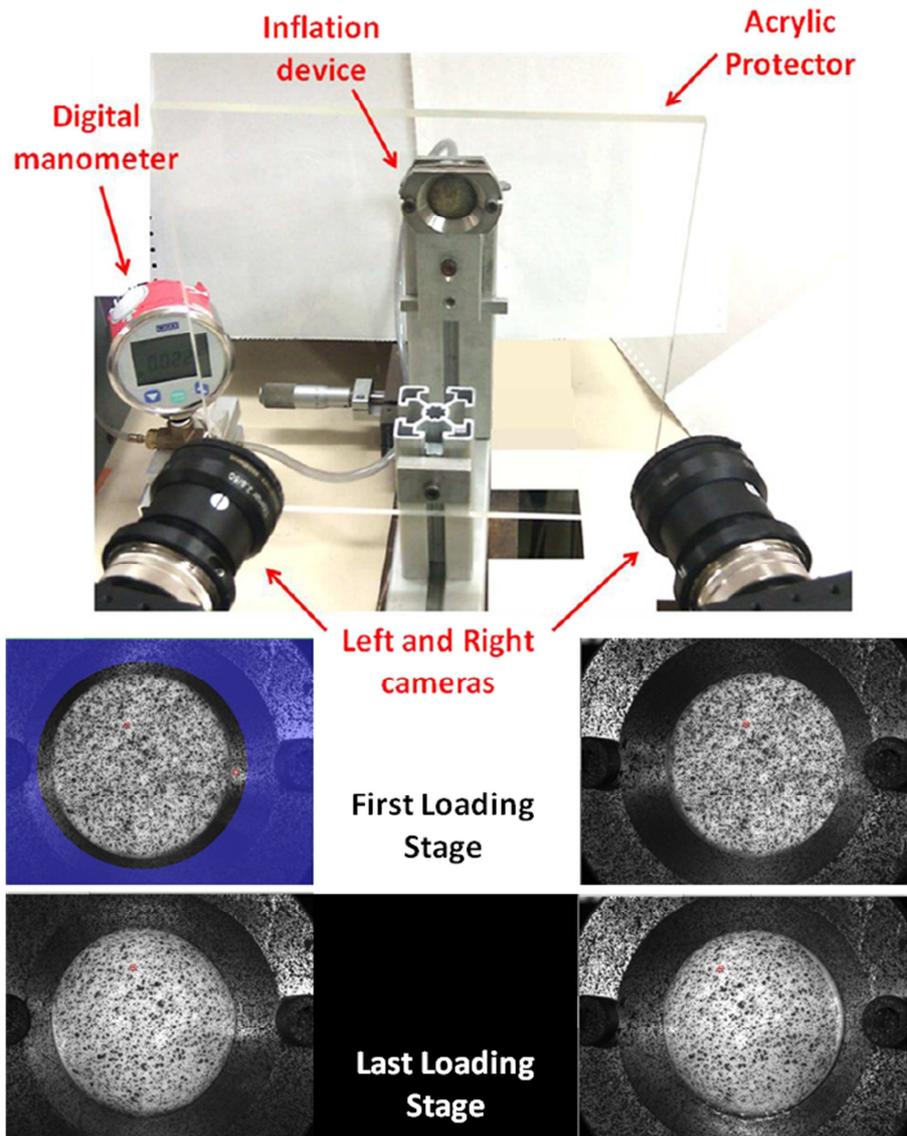
Fig. 2. View of the experimental set-up and the inflation of the ATAA layer through the left and right cameras of the DIS-C system. An image is recorded every loading stage defined at 3 kPa, for the duration of the test. Note that the acrylic protector is used to prevent water from reaching the cameras when the specimen bursts.
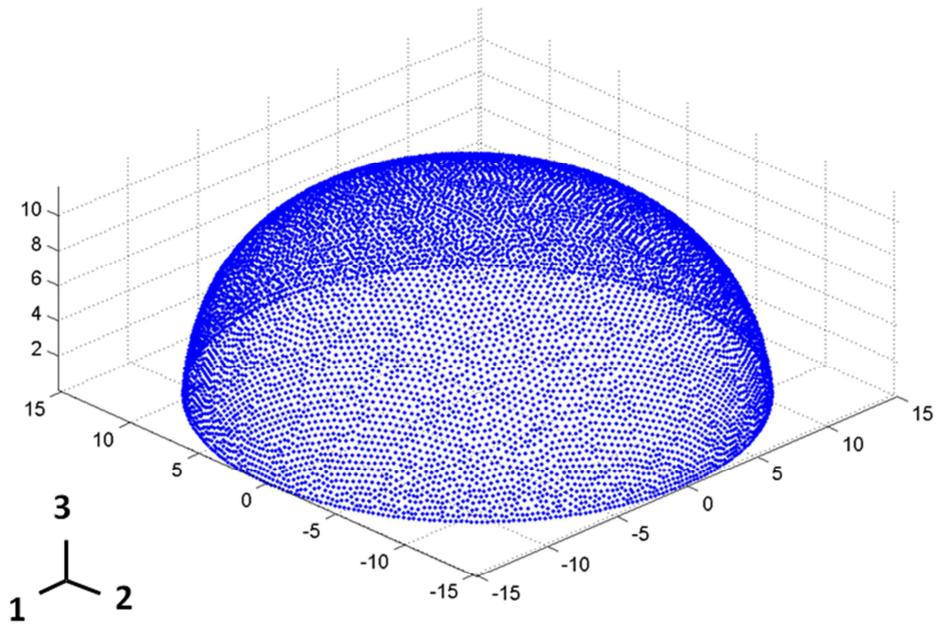
Fig. 3. Reconstructed shape of the ATAA layer at the final inflation stage. The 3D coordinates of each material point were used to reconstruct the shape.
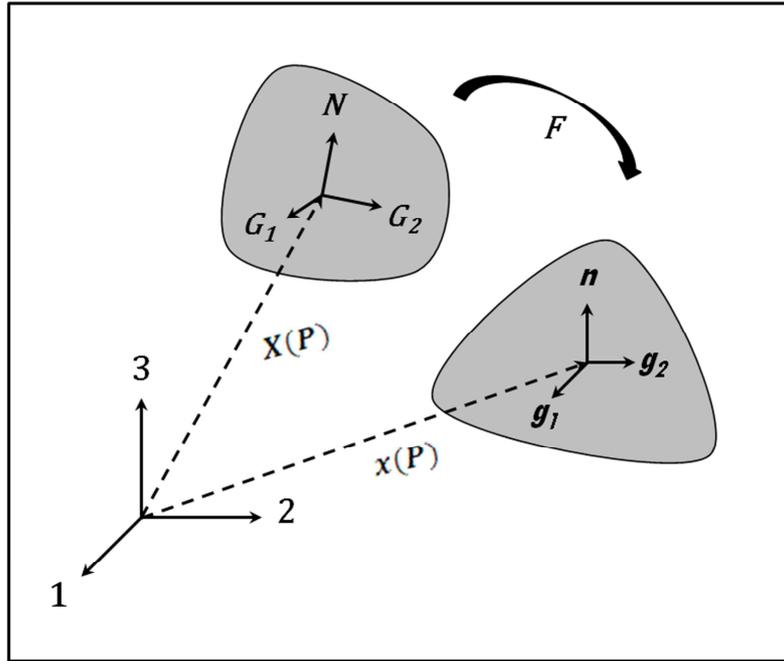
Fig. 4. Schematic of the kinematics and base vectors.
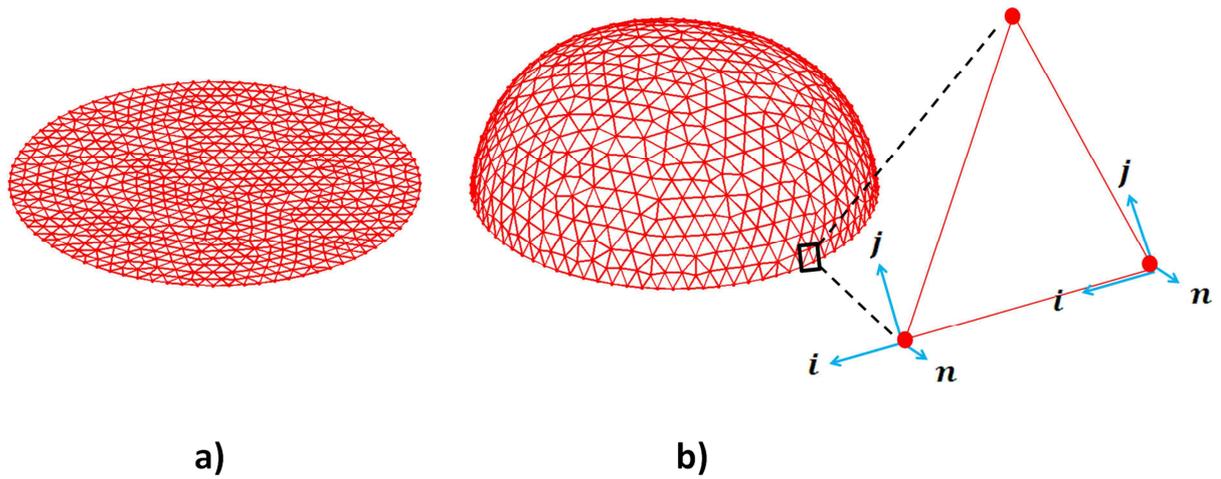
Fig. 5. Discretization of the surface. The unchanged mesh is deformed from a) the initial to b) the current configuration. For one boundary element the local (i, j, n) Cartesian frame used to define the boundary conditions is shown.
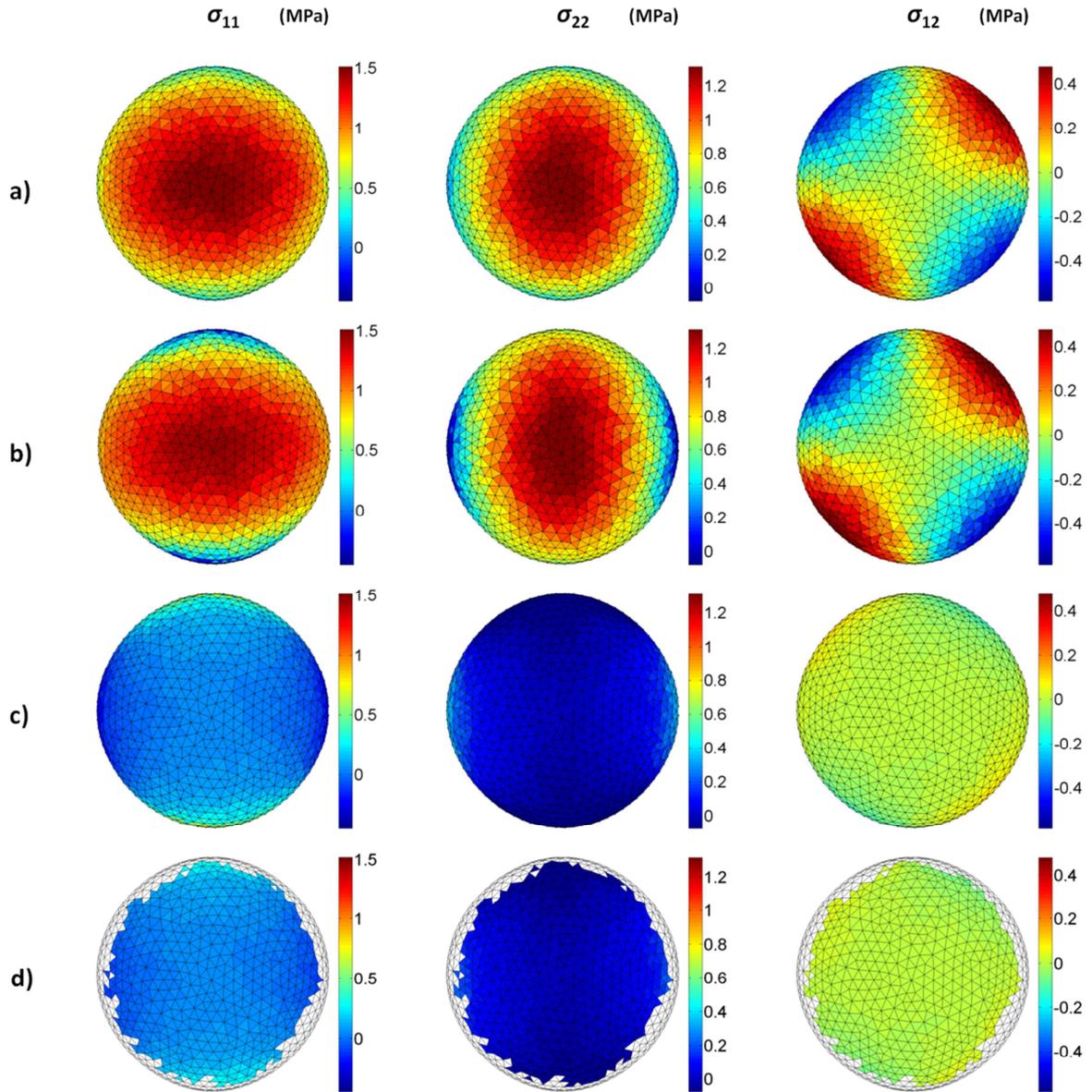
Fig. 6. Top view of the element by element comparison between stress fields calculated by a) the FEA simulation (reference) and b) our approach. The absolute error (in MPa) between a) and b) is presented in c) and in d) where the boundary elements are neglected.
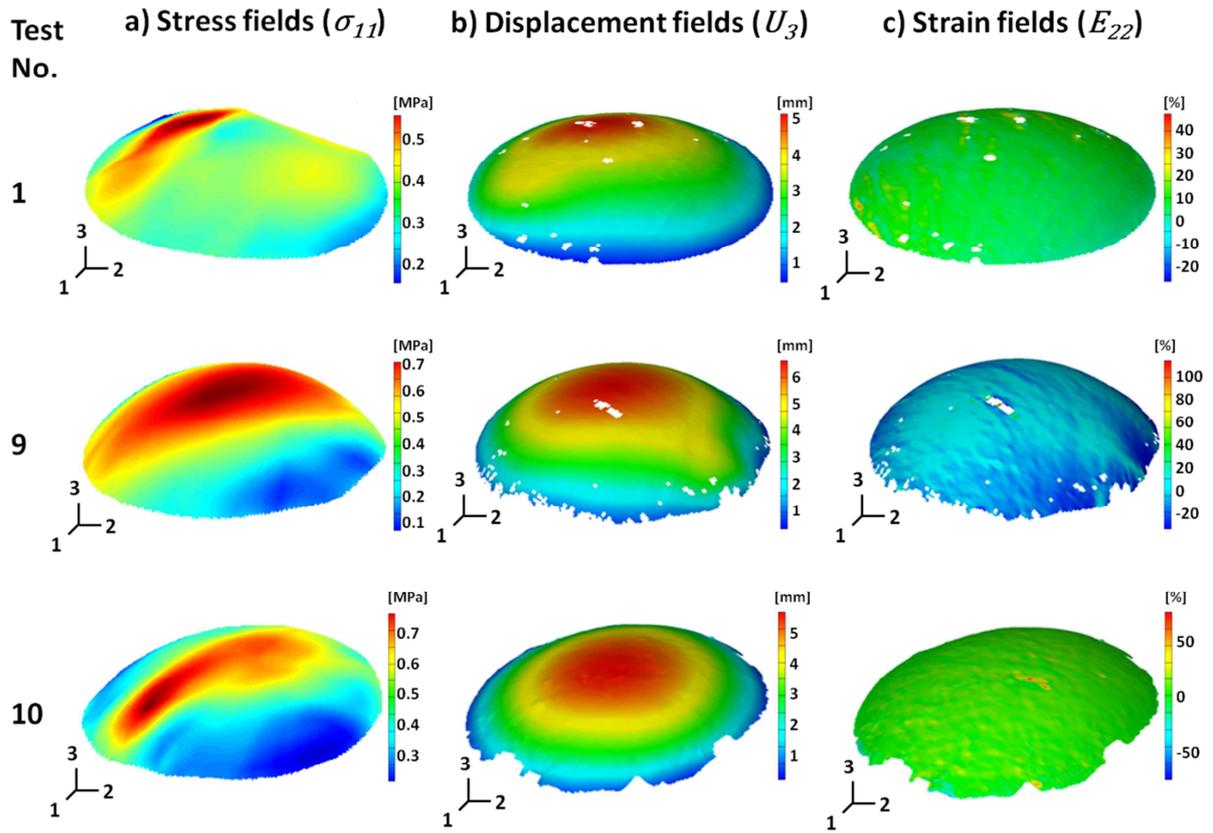
Fig. 7. The a) stress field (σ_{11}), b) displacement field (U_3) and c) strain field (E_{22}) for three ATAA specimens all at a pressure of 0.027 MPa.
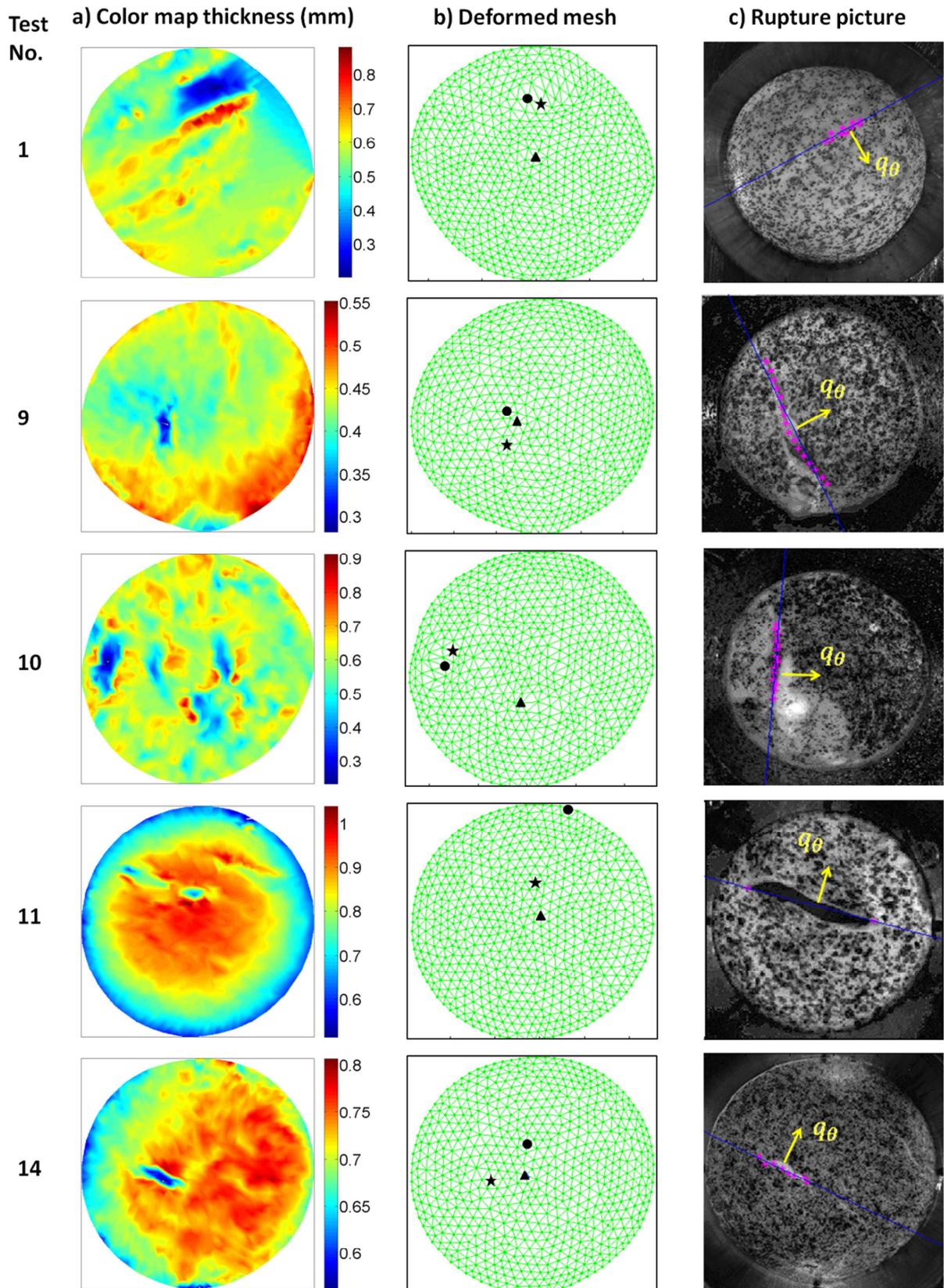
Fig. 8. ATAA rupture. For each test, a) the color map of the thickness measurement, b) the deformed mesh (⬤ = NodeMAX, ▲ = NodeTOP, ★ = NodeRUP) and c) the rupture picture where q_θ is the unit vector perpendicular to the rupture.
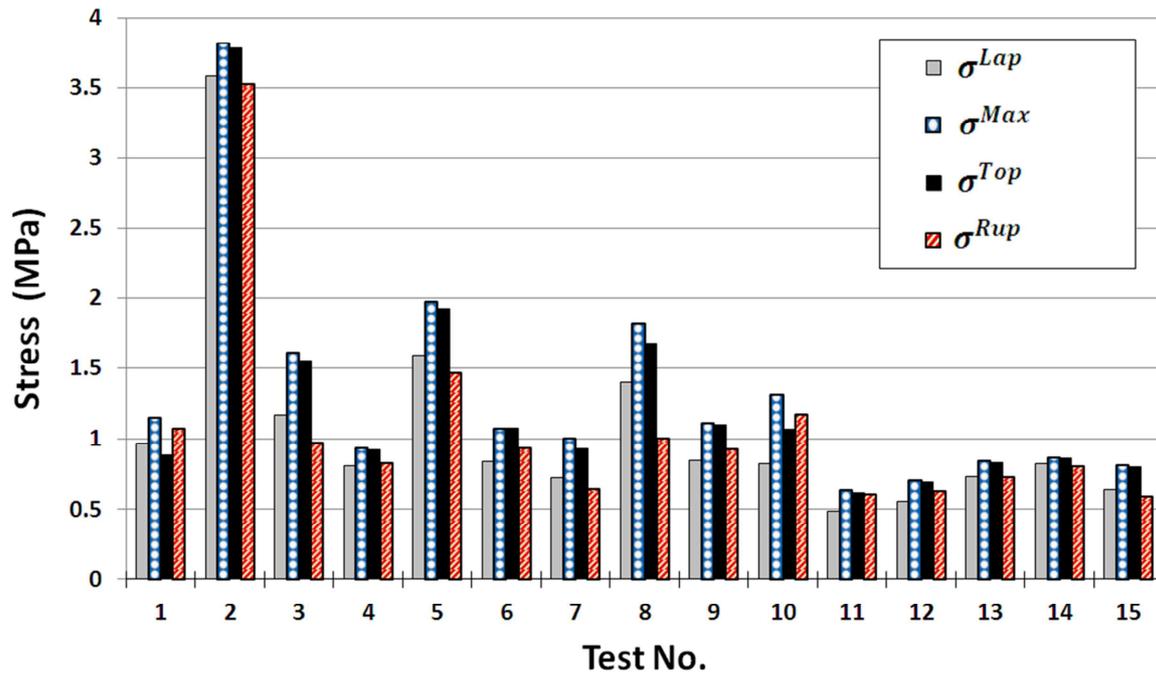
Fig. 9. Four different ultimate stresses for each of the 15 ATAA samples where σ^{Lap} is the Laplace stress calculated from Eq. (12), σ^{Max} is the maximum principal stress, σ^{Top} is the maximum principal stress at the node of the top, and σ^{Rup} is the rupture stress calculated from Eq. (10).

Thickness evolution (mm)

0.003 MPa

0.018 MPa

0.033 MPa

0.048 MPa
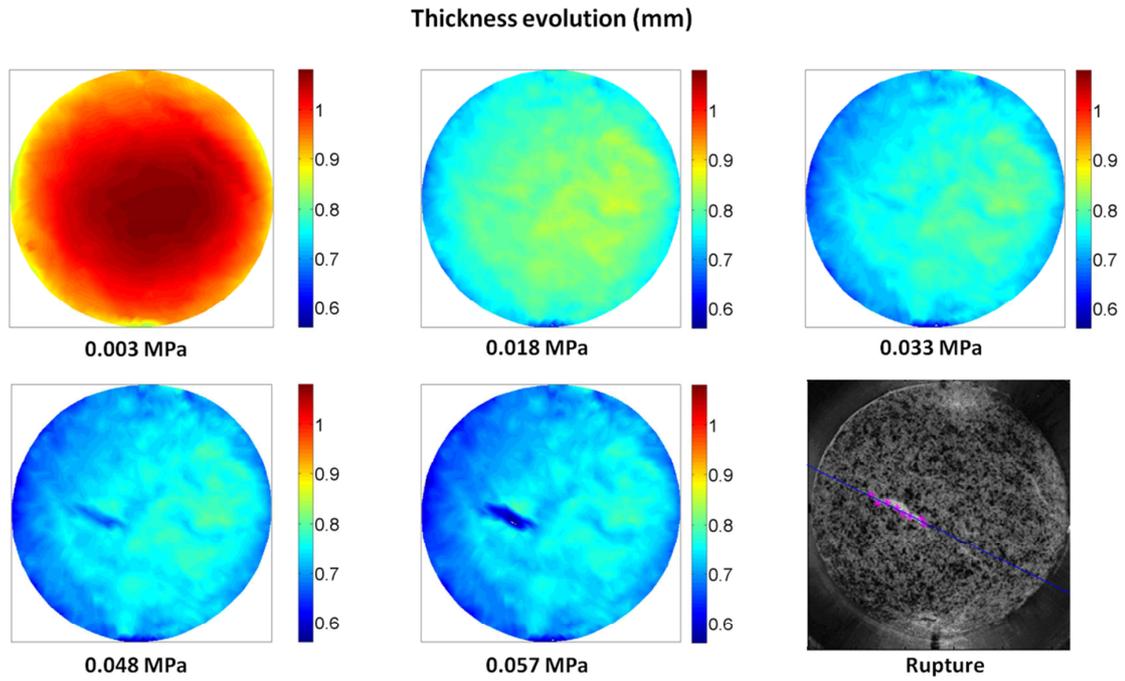
0.057 MPa

Rupture

Fig. 10. Local thickness evolution (Eq. (11)) in mm. for one representative ATAA sample (Test No. 14). Top view from the initial stage (0.003 MPa) until the final stage (0.057 MPa) and the image captured by the DIS-C system at rupture are presented.

APPENDIX A

To validate the membrane assumption the stress fields calculated by our approach on a pre-defined geometry were compared to reference stresses provided by a finite element analysis (FEA) on the same reference geometry. In order to compare exactly the data at the same points, we used the same nodal arrangement for both methods, which means that we had to interpolate the reference FEA results into our own predefined mesh used in our approach (644 nodes and 1203 elements).

Validation Process

A FEA simulation of the inflation process was performed with the aim to numerically reproduce an experimental dataset. Using the Abaqus® software we created a 0.85 mm thick circular patch of 30 mm of diameter, corresponding to the area of interest (AOI) for an inflated of the experimental aortic layers. In order to perform the numerical simulation it was necessary to define the material properties of the circular patch, which were based on the anisotropic hyperelastic Holzapfel-Gasser-Ogden (HGO) model (Holzapfel et al. 2000). The material properties defined for the FEA simulation were obtained from the literature: *density*= 5.0e-4 , C_{10}= 0.0764 MPa, *D*= 1.e-8 , k_1= 0.0839611 MPa, k_2= 1.2644611 , κ= 0 and β= 41 °.

The nodes on the boundary of the circular patch were pinned allowing their rotation. The applied load was defined as a uniform pressure of 0.06 MPa, applied to the inner surface of the circular patch (Fig. A1). Finally the mesh size of the simulation was defined by 10119 nodes and 19887 shell elements.
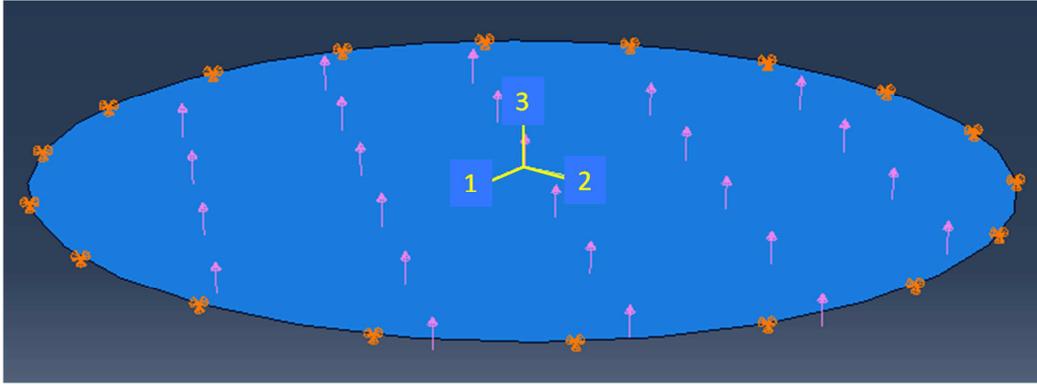
Fig. A1. Lateral view of the circular patch created in Abaqus® software. Boundary conditions allow the rotation. A uniform pressure is applied to the inner surface of the patch.

25

26   The FEA simulation provided the displacement and stress distributions at the end of the inflation. The

27   stress fields provided by this FEA simulation were then used as a reference for the validation of our

28   approach and the final geometry provided by this FEA was also used as the reference geometry for

29   validating our approach.

30

31   For our simulation, we used shell elements which yielded two sets of stress fields in the results, one

32   located at the inner surface (Fig. A2-a) and another located at the outer surface (Fig. A2-b) of the

33   inflated membrane. The stress at the inner surface was slightly lower than the stress at mid-thickness

34   and the stress at the outer surface was slightly higher than the stress at mid-thickness. For a 0.85 mm

35   thick sheet, it was estimated that the mean absolute difference between the stress at the inner and

36   outer surface was 0.32 MPa for σ_{11}, 0.26 MPa for σ_{22} and 0.0013 MPa for σ_{12}. In contrast, our

37   approach provides directly the stress field at mid-thickness. Knowing this, the two stress fields, outer

38   and inner, obtained from the FEA simulation were averaged to provide an accurate comparison with

39   our approach.

40
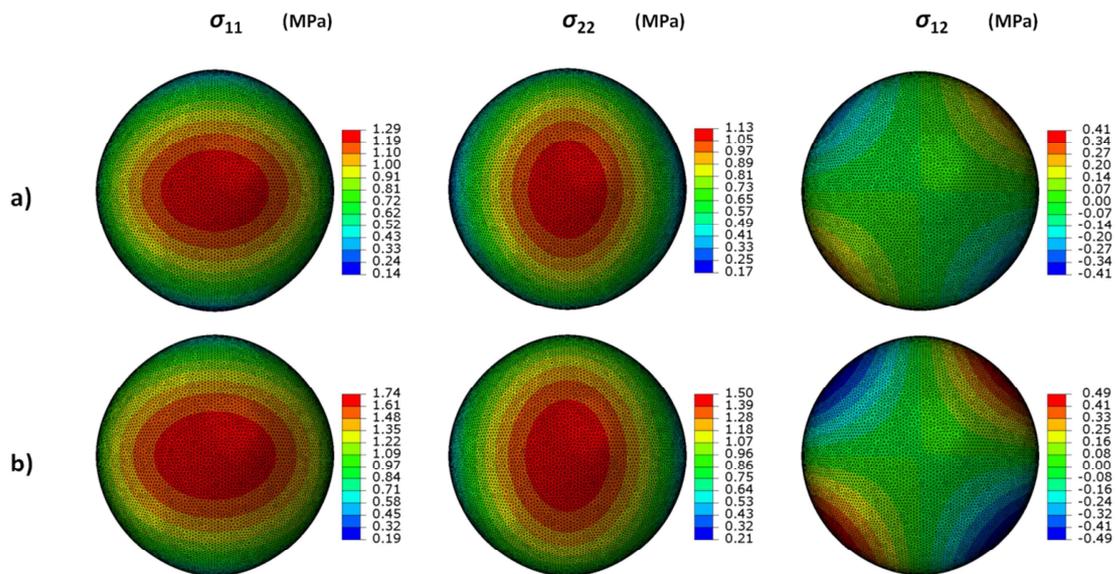
Fig. A2. FEA computation (Abaqus® software top view) provided stress fields located at a) the inner surface and b) the outer surface of the inflated membrane.

41

42   After extracting the nodal displacements, we interpolated the values across a grid of pixels in order

43   to create a dataset with the same spatial resolution as the experimental data (Fig. A3). Then we

44   applied our approach to these experimental-like data in order to reconstruct the maps of the Cauchy

45   stress tensor. Using the Abaqus® output file, we interpolated the stress values at the same nodes

46   that we reconstructed them. Afterwards our Cauchy stress estimates, from applying our approach to

47   the experiment-like data, were compared to the Cauchy stress values provided by the FEA

48   computation.

49
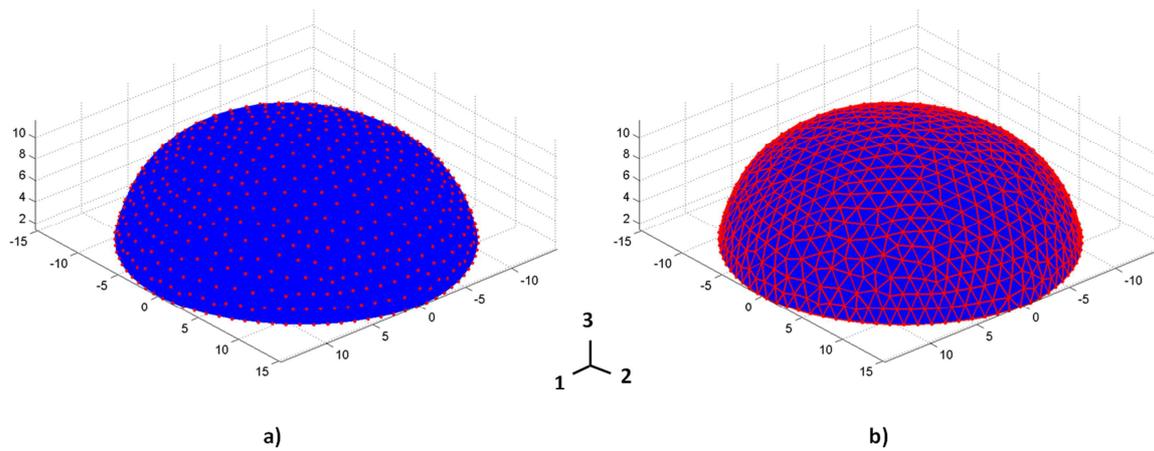
Fig. A3. The 3D deformed geometry (surface) obtained with the FEA simulation (blue) was imported into Matlab®
a) Nodes where the Cauchy stress will be estimated are defined (red dots) across this surface
b) The surface is meshed using the Delaunay triangulation.

50

51   Therefore, we were able to compare, element by element, the results of our approach and those of a

52   reference FEA simulation. In Figure A4-a the reference stress distribution from the FEA simulation is

53   shown and in Figure A4-b the stress distribution from our approach is displayed. The difference

54   between both was calculated at each element and is presented in Figure A4-c. Mean absolute errors

55   of 0.031 MPa for σ_{11}, 0.002 MPa for σ_{22}, and 0.005 MPa for σ_{12}.were calculated between our

56   approach and the FEA simulation. These mean absolute errors are equivalent to mean relative errors

57   of 3.5% for σ_{11}, 0.3% for σ_{22} and 0.5% for σ_{12}.

58
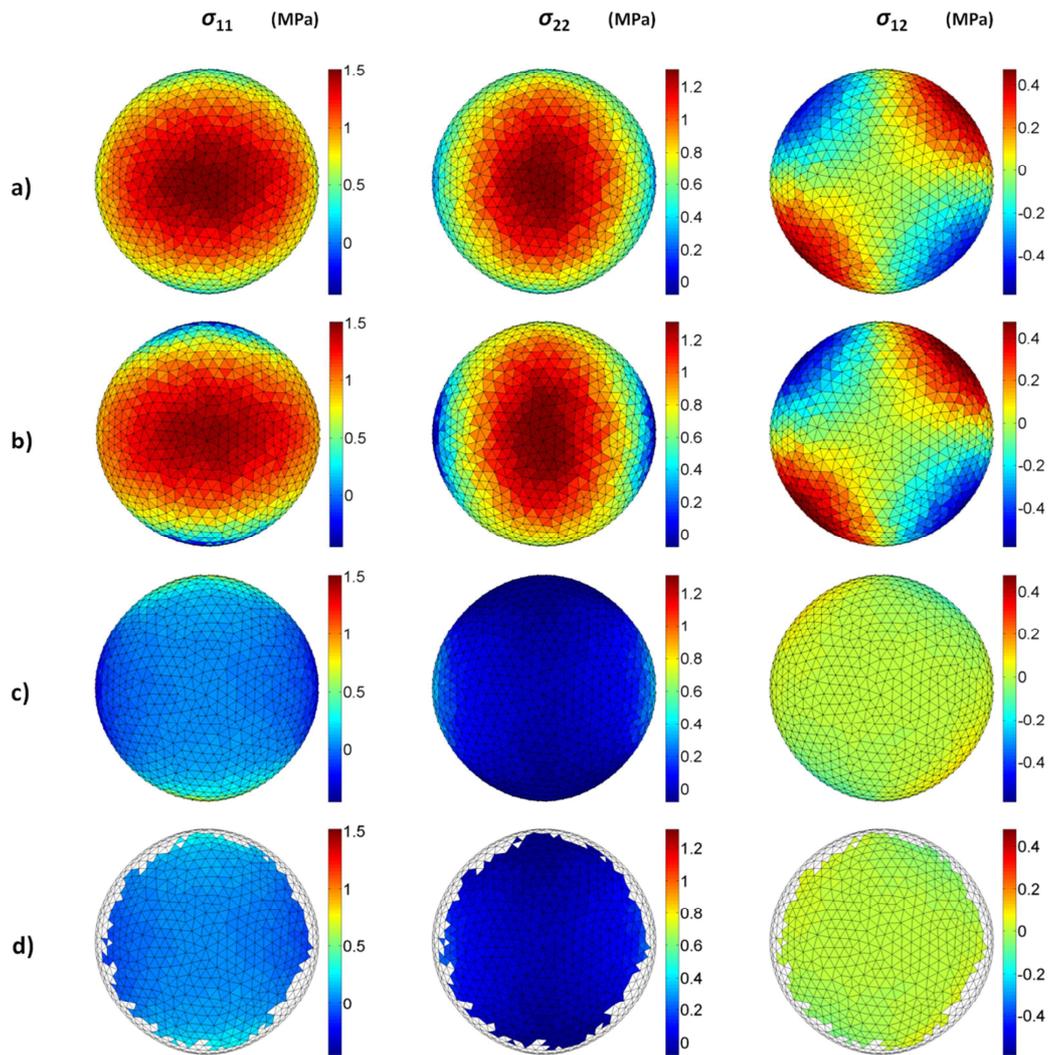
Fig. A4. **Top view of the element by element comparison between stress fields calculated by a) the FEA simulation (reference) and b) our approach. The absolute error (in MPa) between a) and b) is presented in c) and in d) where the boundary elements are neglected.**

59

60   The differences in the results are due to the different boundary conditions used for each method (i.e.

61   pinned for the FEA approach and traction boundary conditions for our approach). An interesting

62   result was that the boundary conditions only affected the estimated stress near the border. After

63   removing the three first stripes of triangles adjacent to the border (Fig. A4-d), the mean absolute

64   errors were reduced to 0.008 MPa for σ_{11}, 0.013 MPa for σ_{22}, and 0.008 MPa for σ_{12}. These mean

65   absolute errors are equivalent mean relative values of 0.8% for σ_{11}, 1.4% for σ_{22} and 0.8% for σ_{12},

66   indicating that the stress estimates contain some errors along the border due to the assumed

67   boundary conditions but these errors vanish rapidly away from the border.